Planetary and Space Science 113-114 (2015) 321–335

Contents lists available at ScienceDirect

Planetary and Space Science

journal homepage: www.elsevier.com/locate/pss

Thermal structure of Venus nightside upper atmosphere measured by stellar occultations with SPICAV/Venus Express

A. Piccialli [a,b,*], F. Montmessin [a], D. Belyaev [c,d], A. Mahieux [e,f,g], A. Fedorova [c,d], E. Marcq [a], J.-L. Bertaux [a], S. Tellmann [h], A.C. Vandaele [e], O. Korablev [c,d]

[a] LATMOS – UVSQ/CNRS/IPSL, 11 bd dAlembert, 78280 Guyancourt, France
[b] Laboratoire d'Études Spatiales et d'Instrumentation en Astrophysique (LESIA), Observatoire de Paris/CNRS/UPMC/ Univ. Paris Diderot, F-92195 Meudon, France
[c] Space Research Institute (IKI), 84/32 Profsoyuznaya, 117810 Moscow, Russia
[d] MIPT, 9 Institutskiy per., 141700 Dolgoprudny, Russia
[e] Planetary Aeronomy, Belgian Institute for Space Aeronomy, 3 av. Circulaire, B-1180 Brussels, Belgium
[f] Fonds National de la Recherche Scientifique, rue dEgmont 5, B-1000 Brussels, Belgium
[g] Department of Planetary Sciences, University of Arizona, 1629 E. University Blvd, Tucson, AZ, 85721, United States
[h] Rheinisches Institut für Umweltforschung, Abteilung Planetenforschung, University of Cologne, Aachener Str, D-50931 Cologne, Germany

ARTICLE INFO

Article history:
Received 26 March 2014
Received in revised form
8 October 2014
Accepted 4 December 2014
Available online 18 December 2014

Keywords:
Venus
Atmosphere
Atmospheres
Structure
Occultations
Spectroscopy

ABSTRACT

The thermal structure of Venus upper atmosphere (90–140 km) was investigated using stellar occultation measurements acquired by the SPICAV experiment on board Venus Express. The SPICAV ultraviolet channel provides CO_2 local density and temperature vertical profiles with a vertical resolution of <7 km of both the southern and the northern hemispheres on the nightside (18:00–06:00 h local time). A permanent layer of warm air is observed at the mesopause in the altitude range 90–100 km. Temperature then decreases with increasing altitude reaching a minimum value around 125 km. Spatial and temporal changes in the thermal structure have been analyzed. Local time variations dominate the structure of Venus atmosphere at these altitudes: temperatures show an increase of $\sim$20 K on the morning side compared to the evening side. The homopause altitude was also determined; it varies between 119 and 138 km of altitude, increasing from the evening side to the morning side. SPICAV temperature profiles were compared to several literature results from ground-based observations, previous spacecraft missions and the Venus Express mission.

1. Introduction

The Venus' upper atmosphere (80–140 km altitude) is one of the most intriguing regions on the planet. It corresponds to a transition region characterized by complex dynamics and circulation: strong retrograde zonal winds (RSZ) dominate the lower mesosphere while a solar-to-antisolar (SS-AA) circulation driven by a day-to-night temperature gradient can be observed in the upper mesosphere/lower thermosphere (Schubert et al., 2007). In addition, photochemical processes, leading to the formation of a sulfuric acid haze (Wilquet et al., 2009), play an important role at these altitudes and affect the thermal structure and chemical stability of the entire atmosphere (Rengel et al., 2008; Clancy et al., 2003; Esposito et al., 1997).

CO_2 density and temperature profiles of Venus upper atmosphere have been measured from both ground-based (Clancy and Muhleman, 1991; Clancy et al., 2003, 2008, 2012; Lellouch et al., 1994; Rengel et al., 2008; Sonnabend et al., 2012) and spacecraft missions: Pioneer Venus (PV) orbiter (Taylor et al., 1980), PV probes (Seiff et al., 1980), Galileo flyby (Roos-Serote et al., 1995), Venera 15 and 16 (Zasova et al., 2006, 2007). Based on these early observations, a Venus International Reference Atmosphere (VIRA) model (Kliore et al., 1985) was published in 1985. The VIRA model presents an atmospheric temperature that decreases from values of $\sim$240 K at the cloud top ($\sim$65 km) to 170 K at $\sim$90–100 km altitudes on the dayside of the planet and reaching minimum

* Corresponding author at: Laboratoire d'Études Spatiales et d'Instrumentation en Astrophysique (LESIA), Observatoire de Paris/CNRS/UPMC/Univ. Paris Diderot, 5, place Jules Janssen F-92195 Meudon, France.
E-mail addresses: arianna.piccialli@latmos.ipsl.fr (A. Piccialli), franck.montmessin@latmos.ipsl.fr (F. Montmessin), dbelyaev@iki.rssi.ru (D. Belyaev), arnaud.mahieux@aeronomie.be (A. Mahieux), fedorova@iki.rssi.ru (A. Fedorova), emmanuel.marcq@latmos.ipsl.fr (E. Marcq), Jean-Loup.Bertaux@latmos.ipsl.fr (J.-L. Bertaux), stellman@uni-koeln.de (S. Tellmann), A-C.Vandaele@aeronomie.be (A.C. Vandaele), Korab@iki.rssi.ru (O. Korablev).

http://dx.doi.org/10.1016/j.pss.2014.12.009
0032-0633/

values of less than 120 K during the nighttime in the upper atmosphere (Keating et al., 1985; Seiff et al., 1985).

More recently, several experiments on board the European mission to Venus, Venus Express (VEx) (Svedhem et al., 2007, 2009; Titov et al., 2009), and ground-based campaigns (Rengel et al., 2008; Clancy et al., 2012; Sonnabend et al., 2012) have extensively studied the thermal structure of Venus upper atmosphere over a long time scale revealing a far more complex situation. A layer of warm air has been detected at altitudes of 90–120 km on the nightside both by SPICAV/VEx and SOIR/VEx (Bertaux et al., 2007a; Mahieux et al., 2012, 2015) and by ground-based observations (Rengel et al., 2008; Sonnabend et al., 2012). Furthermore, the thermal structure of Venus upper mesosphere/lower thermosphere shows a significant variability both on day-to-day as well as on longer timescales (Rengel et al., 2008; Clancy et al., 2012; Sonnabend et al., 2012).

In the present paper, we describe the thermal structure of Venus upper atmosphere observed by the SPICAV-UV experiment in the stellar occultation mode. We briefly describe the SPICAV-UV stellar occultation dataset in Section 2. We review the retrieval technique in Section 3 and then present the results in Sections 4–6. A comparison to several published results from ground-based observations, previous spacecraft missions and the Venus Express mission is included in Section 7.

2. SPICAV-UV stellar occultation dataset

The SPICAV (spectroscopy for the investigation of the characteristics of the atmosphere of Venus) instrument has been operating on board the ESA orbiting platform Venus Express since 2006 (Svedhem et al., 2007, 2009; Titov et al., 2009). A detailed description of the SPICAV instrument as well as its scientific objectives can be found in Bertaux et al. (2007a). SPICAV is a remote sensing spectrometer covering distinct spectral regions in ultraviolet (118–320 nm) and near-infrared (650–1700 nm). In the occultation mode the UV sensor is particularly well suited to measure the vertical profiles of CO_2, temperature, SO_2, SO, clouds and aerosols of the middle and upper atmosphere of Venus between typically 80 and 140 km of altitude (Bertaux et al., 2007b; Montmessin et al., 2011; Belyaev et al., 2012). During a stellar occultation the instrument points tangentially through the atmosphere toward a star which is observed through the atmosphere as it rises or sets. When the star is seen through the atmosphere, the light is absorbed by all atmospheric constituents, allowing derivation of vertical profiles of CO_2 (from which local density and temperature can be inferred), ozone and aerosols (Quémerais et al., 2006; Montmessin et al., 2006; Forget et al., 2009). The ultraviolet sensor of SPICAV has a sampling of 0.54 nm and a spectral resolution varying from 1 to 2.5 nm. The vertical resolution obtained in stellar occultation ranges from 500 m to ~7 km, depending on the grazing configuration of the SPICAV line of sight (LOS). A typical occultation lasts for 30 min during which a reference stellar spectrum is assembled based on the average of all stellar spectra acquired above a tangential altitude of 250 km (Fig. 1).

A stellar occultation profile is spread over a latitude and longitude interval smaller than 2°, the reference location for each profile being determined at an altitude of 85 km. For this study we analyze data from more than 587 stellar occultations acquired by SPICAV-UV between December 2006 and February 2013. Fig. 2 shows the latitudinal and the local time coverage of the stellar occultation profiles used for this study. The observations cover all latitudes on the nightside between 18:00 and 06:00. Three profiles have a local time higher than 07:00 h, however they were acquired during the Venus polar night corresponding to a solar zenith angle of ~83–85°.

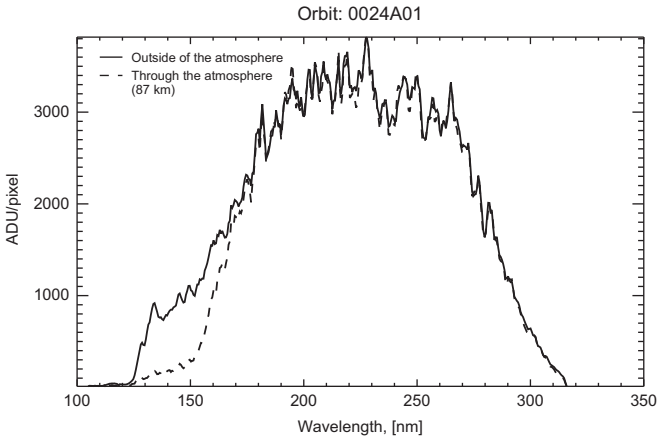

Fig. 1. (Solid line) Spectrum of the star obtained outside of the atmosphere and taken as reference spectrum. (Dashed line) Spectrum of star acquired through the atmosphere at an altitude of about 87 km.

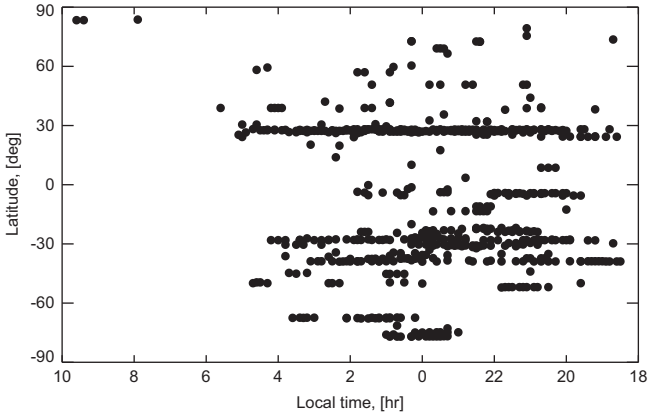

Fig. 2. Latitudinal and local time distribution of the 587 stellar occultation profiles used for this paper.

3. Retrieval method description

3.1. Column densities

As described in Royer et al. (2010), the measured spectrum of the star includes the atmospheric absorptions, like ozone and aerosol, as well as nitric oxide (NO) airglow emitted on the nightside. The stellar occultation retrieval consists first in separating the nitric oxide emission from the stellar spectrum to allow further derivation of the wavelength-dependent atmospheric transmission determined for each sounded altitude. Using the same retrieval method as in Quémerais et al. (2006) and Montmessin et al. (2006), LOS integrated densities (slant densities) for CO_2, O_3 and aerosols are retrieved. In the remainder of this paper, only CO_2 is considered.

3.2. Error estimates

A standard formulation for the signal-to-noise ratio (SNR or alternatively S/N) of a well-behaved charge-coupled device such as the one equipping the UV channel of SPICAV can be found in

Howell (2006)

$$\frac{S}{N}=\frac{N_*}{\sqrt{(N_*+N_s+N_D+N_R^2)}}$$

with N_* being the number of photons created by the star, N_s the number of photons generated by the background (in this case, the nitric oxide emissions), N_D the number of electronics from the dark current and N_R the number of electronics resulting from read noise. Because the number of photons detected by the CCD depends on the overall gain G of the detector, this equation can be reformulated as

$$\frac{S}{N}=\frac{n_*G}{\sqrt{(n_*+n_s)G+n_D/g+N_R^2}}$$

where the reduced variables n_*, n_D and n_s denote the corresponding analog-to-digital unit (ADU) values returned by the A/D converter. The readout noise term has been estimated around 6 ADU, whereas a typical stellar spectrum produces an average level of 2000 ADU, and the dark current an average of 400 ADU (when the Peltier cooler is not set). The overall gain G varies between 0.3 and >12 (the number of ADU per photo-events) and is adjusted during observation planning so as to maintain the same signal level at the detector output depending on the brightness of the targeted star. From this formula, each pixel can be assigned a corresponding $1-\sigma$ uncertainty that comprises the various sources of noises. In the case of stellar occultation, the spectra are divided by the reference stellar spectrum obtained from the average of 1000 individual spectra. With such averaging, the noise contribution of the reference spectrum is almost negligible and the final error on atmospheric transmission is taken equal as the spectrum errors divided by the reference stellar value for the same pixel.

For each collected transmission, an associated error spectrum is given to the spectral inversion Levenberg–Marquardt (LM) routine that minimizes the Chi-square value based on the estimated error bars. Resulting uncertainties for the retrieved parameters (slant densities) are a by-product of the LM routine, being inferred from the square-root of the diagonal elements of the covariance matrix. Error is further propagated to local quantities, as explained below.

3.3. Local densities and temperature

The relation between the CO_2 slant density N_i (cm^{-2}) and the local density n_l (cm^{-3}) at the point l along the LOS is given by

$$N_i=2\int_0^{\infty} n_l\,dl=2\int_0^{\infty}\frac{P_l}{kT_l}\,dl \tag{1}$$

where l is an abscissa along the LOS, P_l is the CO_2 pressure (Pa), T_l is the temperature (K), and k is Boltzman's factor (1.38×10^{-23} J/K). The atmosphere is assumed to be spherically symmetric along the line of sight. Eq. (1) can be rewritten by dividing the LOS in $n-i+1$ layers, where n is the number of measurements

$$N_i=\frac{2}{k}\sum_{j=i}^{n}\int_{l_j}^{l_j+\Delta l_j}\frac{P_l}{T_l}\,dl$$

Each layer j has a depth Δl_j defined by

$$\Delta l_j=l_{j+1}-l_j=\sqrt{(R_{Venus}+z_{j+1})^2-(R_{Venus}+z_i)^2}-\sqrt{(R_{Venus}+z_j)^2-(R_{Venus}+z_i)^2}$$

Assuming hydrostatic equilibrium and that each layer is isothermal, then the temperature and the pressure can be expressed respectively as

$$T_l=\overline{T_j}\quad\text{for } l\in[l_j,l_j+\Delta l_j],\qquad P_l=P_{j+1}\exp\left(\frac{-(z_l-z_{j+1})}{H_j}\right)$$

where $\overline{T_j}$ is the average of the temperature within the layer j, $H_j=R\overline{T_j}/mg_j$ is the scale height, and g_j was chosen such that $g_j=g_0(R_{Venus}/(R_{Venus}+z_{1/2}^j))^2$ with $z_{1/2}^j$ being the height in the middle of the layer j, and R_{Venus} is the Venus radius (6051.5 km). The CO_2 slant density N_i can then be written a:

$$N_i=\frac{2}{k}\sum_{j=i}^{n}\overline{T_j^{-1}}\int_{l_j}^{l_j+\Delta l_j}P_{j+1}\exp\left(\frac{-(z_l-z_{j+1})}{H_j}\right)dl \tag{2}$$

The index j increases from the layer of impact point ($j=i$) to the layer closest to the spacecraft ($j=n$). The integration over l does not admit a simple analytic formulation, therefore it is necessary to integrate numerically by using the trapezoidal rule or the Gaussian quadrature. By applying the second method, Eq. (2) can then be written as

$$N_i=\frac{2}{k}\sum_{j=i}^{n}\overline{T_j^{-1}}\sum_{k=1}^{n_g}w_kP_{j+1}\exp\left(\frac{-(z_{l_k}-z_{j+1})}{H_j}\right) \tag{3}$$

where n_g is the number of points used for the Gaussian quadrature (we chose $n_g=2$, value optimized on a base time calculation/precision), w_k and z_{l_k} are respectively the weights and the altitudes of the Gaussian points. By assuming an initial temperature at the upper layer of the atmosphere ($j=n$), it is then possible to determine the atmospheric thermal profile by integrating from the top to the bottom of the profile and from layer to layer (in this case, P_{j+1} and H_j are known if $j>i$). At each level i, the only unknown is T_i which is adjusted in order to reproduce the observed N_i. T_i is the root of the following equation:

$$\frac{2}{k}T_i^{-1}\sum_{k=1}^{n_g}w_kP_{i+1}\exp\left(\frac{-(z_{l_k}-z_{j+1})mg_i}{RT_i}\right)=N_i-\frac{2}{k}\sum_{j=i+1}^{n}\overline{T_j^{-1}}\sum_{k=1}^{n_g}w_kP_{j+1}\exp\left(\frac{-(z_{l_k}-z_{j+1})}{H_j}\right)$$

This relationship can be solved by using a simple Newton routine. Once T_i is calculated, it is then possible to derive $P_i=P_{i+1}\exp((-(z_i-z_{i+1})mg_i)/RT_i)$ and n_i.

The uncertainty on the temperature is derived by its covariance matrix defined as

$$\mathrm{cov}T=\left(N_T^TE_N^{-1}N_T\right)^{-1}$$

where

$$N_T=\begin{pmatrix}\partial N_1/\partial T_1 & \partial N_1/\partial T_2 & \dots & \dots & \partial N_1/\partial T_n\\ 0 & \dots & \dots & \dots & \dots\\ \dots & \dots & \partial N_i/\partial T_i & \dots & \dots\\ 0 & \dots & 0 & \dots & \partial N_{n-1}/\partial T_n\\ 0 & 0 & \dots & 0 & \partial N_n/\partial T_n\end{pmatrix}$$

and E_N is the covariance matrix of the measurement (assumed to be diagonal and containing the estimated variance of CO_2 slant density at each altitude).

4. Thermal structure of the Venus upper atmosphere

Typical density and temperature profiles of the Venus upper atmosphere between 80 and 150 km altitude for three different latitudes are shown in Fig. 3. The uncertainties on temperature vary with altitude. Typical temperature error values are 1–20 K in the altitude range 100–130 km; at lower (<100 km) and higher (>130 km) altitudes larger errors are observed, 5–60 K. For this study, only temperature values with a relative error less than 25% are considered. Density profiles present at all latitudes a similar behavior with a change in the slope observed between 110 and 130 km of altitude. A change in the curvature of the CO_2 density is present also in the SOIR/VEx data between 120 and 140 km, although it is more pronounced compared to the SPICAV data (Mahieux et al., 2012, 2015). A permanent warm area appears

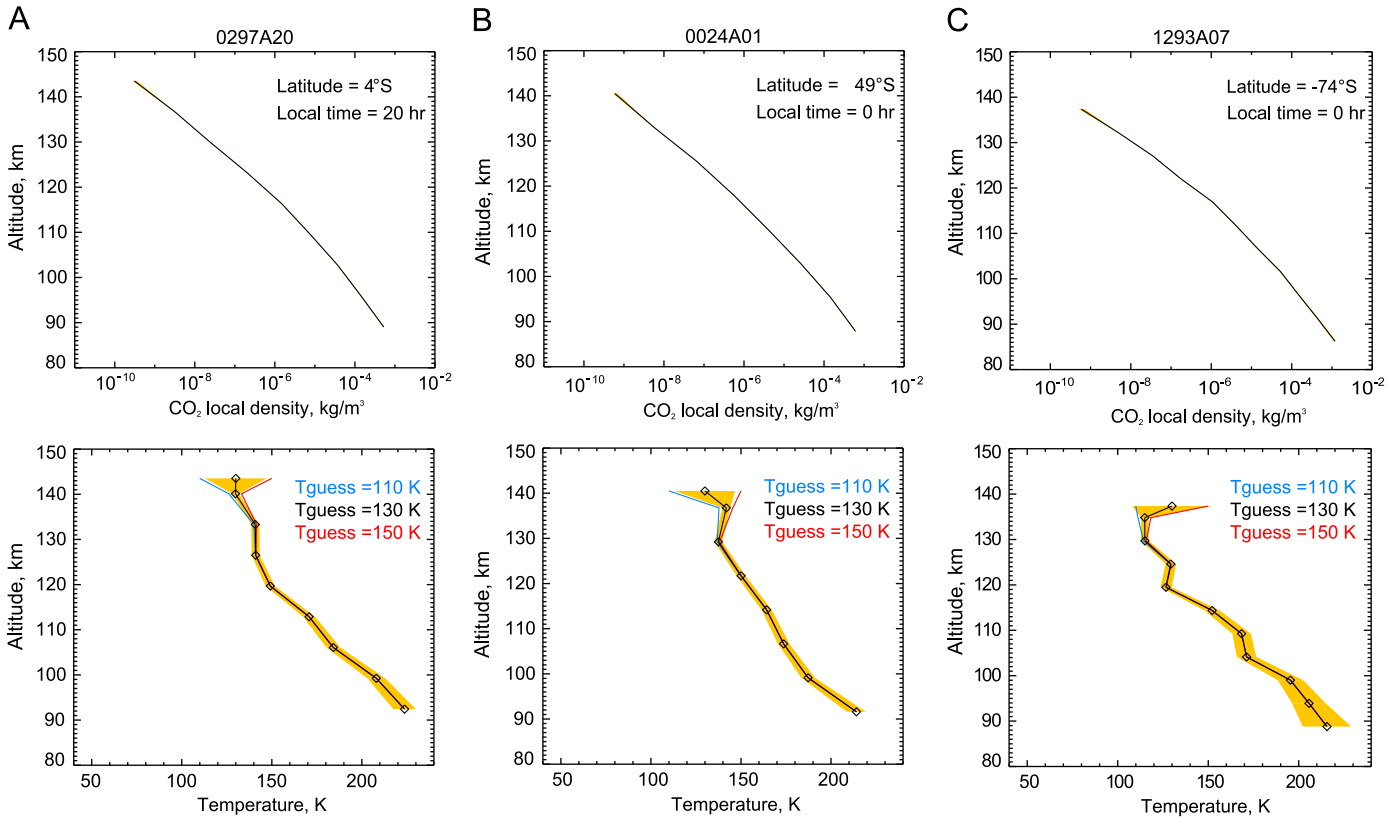

Fig. 3. Example of three sets of density and temperature profiles: (A) equatorial measurement (orbit 0297A20); (B) middle latitude measurement in the north hemisphere (orbit 0024A01); and (C) south polar measurement (orbit 1293A07). The three top panels show CO_2 density profiles. The three panels at the bottom show their corresponding temperature profiles. For each measurement, three profiles, calculated with a prescribed upper boundary temperature of 110, 130, and 150 K (blue, black, and red curves respectively), are shown. The three profiles merge at approx. 125–130 km. The yellow shaded area represents the error on both density and temperature. (For interpretation of the references to color in this figure caption, the reader is referred to the web version of this paper.)

distinctly at the mesopause at about 90–100 km of altitude in all temperature profiles. As a first explanation, this feature was interpreted as the result of adiabatic heating in the downwelling branch of the solar-antisolar thermospheric circulation on the nightside (Bertaux et al., 2007b). The change of curvature observed in the density profiles corresponds to a temperature minimum around 125 km. In the following, we discuss the latitudinal and the temporal variability of both the temperature and the density structure.

4.1. Latitudinal and temporal variations of temperature

Fig. 4 shows maps of Venus thermal structure as a function of latitude and local time at different altitudes. Above 100 km of altitude temperature on the morning side is usually warmer than on the evening side. By comparing the temperature retrieved in the north and south hemispheres of the planet, we observe a symmetry between the two hemispheres, as it was also observed by the VIRTIS and SOIR instruments on board Venus Express (Migliorini et al., 2012; Mahieux et al., 2012).

The latitude–altitude temperature field retrieved by SPICAV stellar occultations is shown in Fig. 5 (top). In order to plot contours of temperature field, individual profiles were first interpolated to a standard altitude grid chosen to retain as much detail of the original dataset as possible, and then were binned on a 5° latitudinal grid. Fig. 5 (bottom) shows the number of profiles for each latitudinal bin; spurious structures present in the temperature field are mainly due to the low sampling. Profiles from the north and the south hemispheres were combined together. The main features that can be clearly observed in the temperature structure are: (i) the warmer layer at 90–100 km altitude, (ii) the constant decrease of temperature with altitude reaching minimum values of ~100–130 K above 120 km altitude. Temperature profiles do not present a significant latitudinal dependence.

Local time variations dominate the structure of Venus atmosphere at these altitudes as can be observed in Fig. 6 (top). Data from northern and southern hemispheres were considered, assuming symmetry. Each profile was first interpolated to a standard altitude grid and then it was binned on a 15 min local time grid. Temperature is warmer on the morning side for altitudes above 95 km. This behavior is better displayed in Fig. 7, where atmospheric temperature at constant altitudes is shown as a function of local time. Temperature appears to be ~20 K warmer at dawn compared to dusk.

In order to remove the influence of variations in CO_2 density, we plotted the cross section of temperature as a function of local time (h) and pressure (mbar) (Fig. 6 (bottom)). Profiles were first interpolated to a standard pressure grid, and then they were binned on a 15 min local time grid. Temperatures in Fig. 6 (bottom) present no dependence on local time thus suggesting that the same altitude does not correspond to the same pressure depending on the local time and that the variability with local time observed in Fig. 6 (top) is mainly due to an expansion of the atmosphere on the morning side.

4.2. Temporal variations of CO_2 density

Local time variations can be also seen on density profiles. Fig. 8 shows the altitude variations of two constant CO_2 density levels (10^{-4} and 10^{-6} kg m^{-3}) as a function of local time for several latitudinal ranges. At the equator (30°S–30°N) the altitudes of both CO_2 density levels increase of ~10 km from evening to morning.

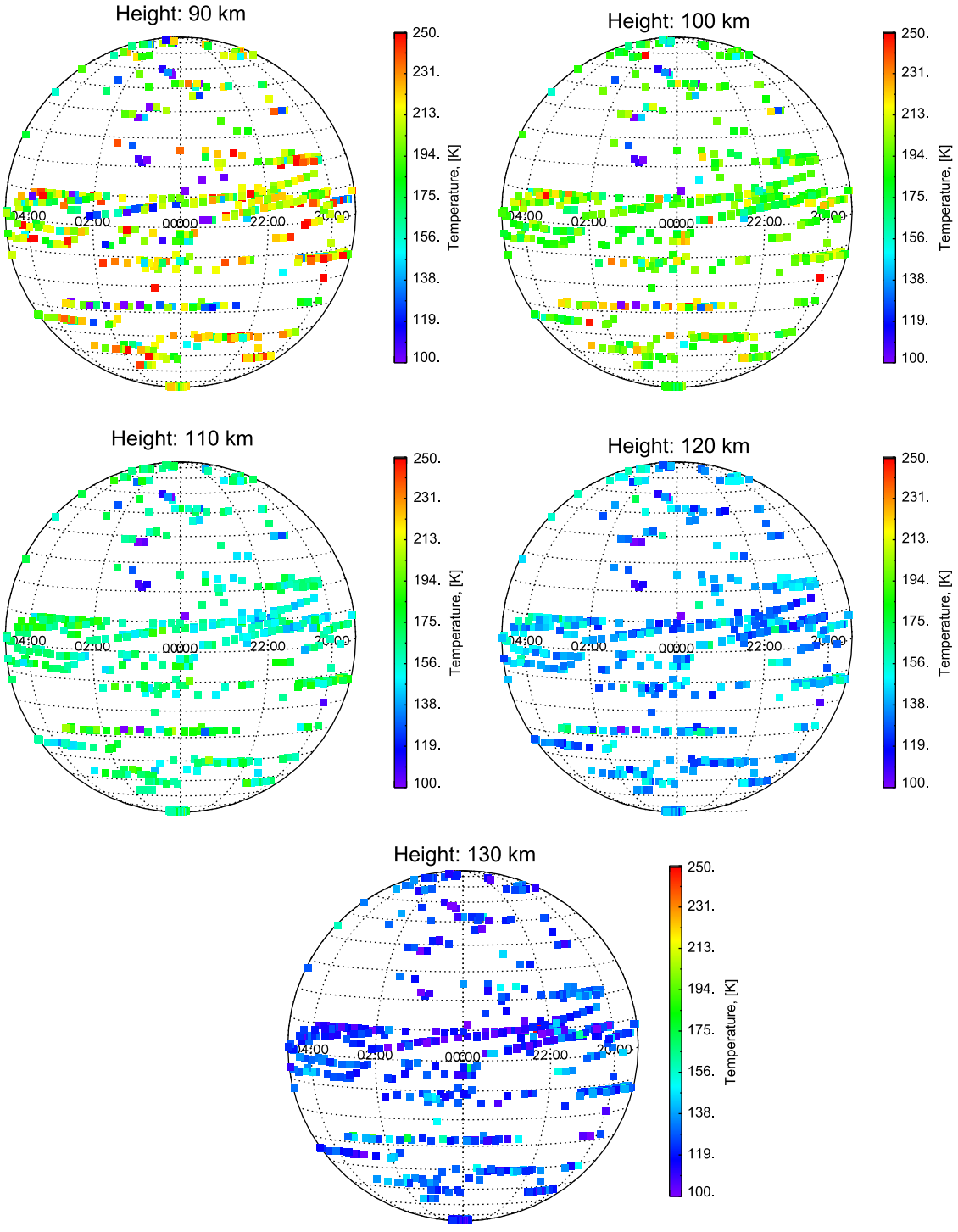

Fig. 4. Global maps of SPICAV temperature as function of latitude and local time at different altitudes.

At other latitudinal ranges altitudes of the CO_2 density levels do not appear to change with local time.

Strong orbit-to-orbit variability is observed both on density and temperature profiles. Fig. 9 shows the altitude of two CO_2 mass density levels (10^{-4} and 10^{-6} kg m^{-3}) as a function of orbit number for different latitudinal bins. For a constant density, altitude variations can reach a maximum value of 18 km, which corresponds to about 4 scale heights (assuming that the scale height H is ~4 km (Lee et al., 2012; Mahieux et al., 2012)).

The CO_2 density profiles, respectively, for the orbit numbers 1415–1515 and 1670–1830, all within the latitude range 30°S–30°N, are presented in Fig. 10. The CO_2 density profiles show a strong variability as a function of both local solar time and orbit number. These variations on the CO_2 density correspond to changes on the temperature profiles of ~10 K on timescales of 24 h up to ~50 K on timescales of few (Earth) months. Such large variations of atmospheric temperature and density were also reported by previous ground-based observations (Rengel et al., 2008; Clancy et al., 2012; Sonnabend et al., 2012) and space experiments (Roos-Serote et al., 1995; Mahieux et al., 2012) and are supposed to be the result of a strong turbulence which occurs in the transition region between the zonal superrotation and the subsolar-to-antisolar flow (Sonnabend et al., 2012).

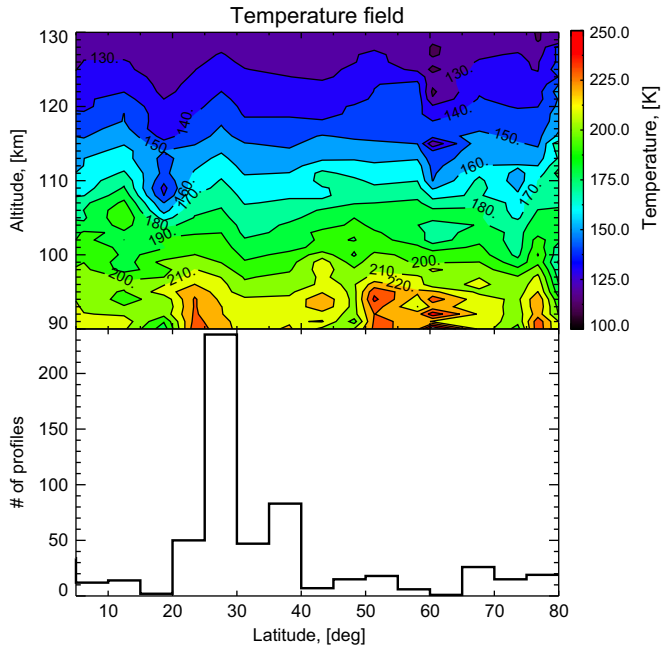

Fig. 5. (Top) Contours of temperature field (K) obtained combining 587 SPICAV profiles. Hemispherical symmetry and local time independence has been assumed. Contours have been smoothed. Contours interval is 10 K. (Bottom) Number of temperature profiles for each latitudinal bin.

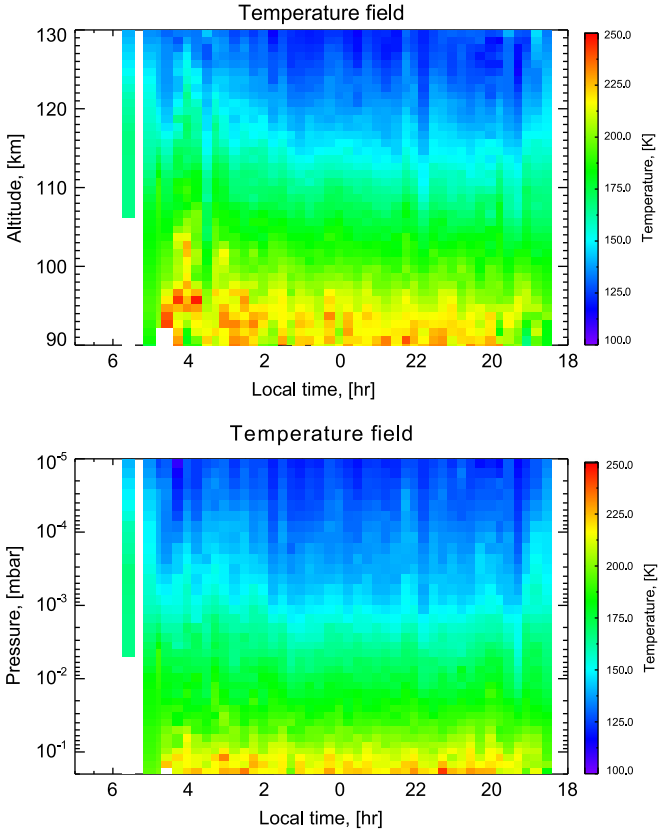

Fig. 6. (Top) Local time-altitude cross section of atmospheric temperature (K) obtained combining the whole SPICAV dataset. (Bottom) Local time-pressure cross section of atmospheric temperature (K). Only temperatures with a relative error less than 25% have been taken in account.

5. Static stability

The static stability is the ability of a fluid at rest to become turbulent or laminar due to the effects of buoyancy. High values of static stability indicate a stable stratified atmosphere, while negative values represent an atmosphere that is unstable against convective overturning. The static stability is quantified as the difference between the measured temperature gradient dT/dz and its dry adiabatic lapse rate Γ_d (Holton, 2004)

$$S = \frac{dT}{dz} - \Gamma_d \tag{4}$$

where z is the geometric height of the atmosphere above the mean radius. The adiabatic lapse rate Γ_d is defined as

$$\Gamma_d = -\frac{g}{C_p} \tag{5}$$

where C_p is the specific heat. The variation of C_p with temperature in Venus atmosphere is taken into account by following the same method as the one described in Lebonnois et al. (2010). Fig. 11 displays vertical profiles of the static stability for different latitudes.

The atmosphere is stable at all altitudes (90–140 km) and latitudes as already observed by previous observations (Tellmann et al., 2009; Seiff et al., 1980) at slighter lower altitudes. This behavior is expected since the mesosphere is mainly a radiative layer, in which convective motions are negligible (Sánchez-Lavega et al., 2008).

6. CO_2 homopause altitude

The homopause, as defined by Nagy et al. (2009), is a transition region in which the vertical distribution of each molecular species changes from being described by the hydrostatic scale height to being described by its individual scale height. Here, we approximate the homopause as the level where the molecular and eddy mixing processes become equally important (Sanchez-Lavega, 2011; de Pater and Lissauer, 2001). Eddy processes dominate the atmosphere below the homopause; this region is known as the homosphere, a layer where the composition is homogeneous and does not vary with altitude due to the mixing produced by different dynamical processes. In the region above the homopause, the heterosphere, molecular diffusion processes become important and each compound assumes its own scale height according to its molecular weight. We derived the homopause altitude by following a method similar to that applied by Mahieux et al. (2012). The molecular diffusion coefficient of CO_2 (D_{CO_2}) is written as (Mahieux et al., 2012)

$$D_{CO_2} = \frac{3 \times 10^2 \cdot \pi \cdot \sqrt{2}}{16} \cdot l_{CO_2} \cdot \nu^{th}_{CO_2}$$

With l_{CO_2} the free mean molecular path

$$l_{CO_2} = \frac{1}{Q_{CO_2} \cdot \rho_{CO_2}}$$

And $\nu^{th}_{CO_2}$ the mean molecular thermal speed

$$\nu^{th}_{CO_2} = \sqrt{\frac{3 \cdot k_B \cdot T \cdot N_{Av}}{MM_{CO_2}}}$$

where Q_{CO_2} is the CO_2 effective cross section (0.52 nm^2), $\rho_{CO_2}(z)$ is the CO_2 volume density (cm^{-3}), k_B is the Boltzmann constant (1.38×10^{-23} J/K), N_{Av} is the Avogadro number (6.02×10^{23} mol^{-1}), and MM_{CO_2} is the CO_2 molar mass (44.01 g/mol).

The eddy coefficient is defined as (Brecht et al., 2012)

$$K = \frac{5.5 \times 10^{12}}{\sqrt{\rho}}$$

where $\rho(z)$ is the total volume density (cm^{-3}) given by $\rho = \rho_{CO_2}/VMR_{CO_2}$. $VMR_{CO_2}(z)$ is the CO_2 volume mixing ratio and

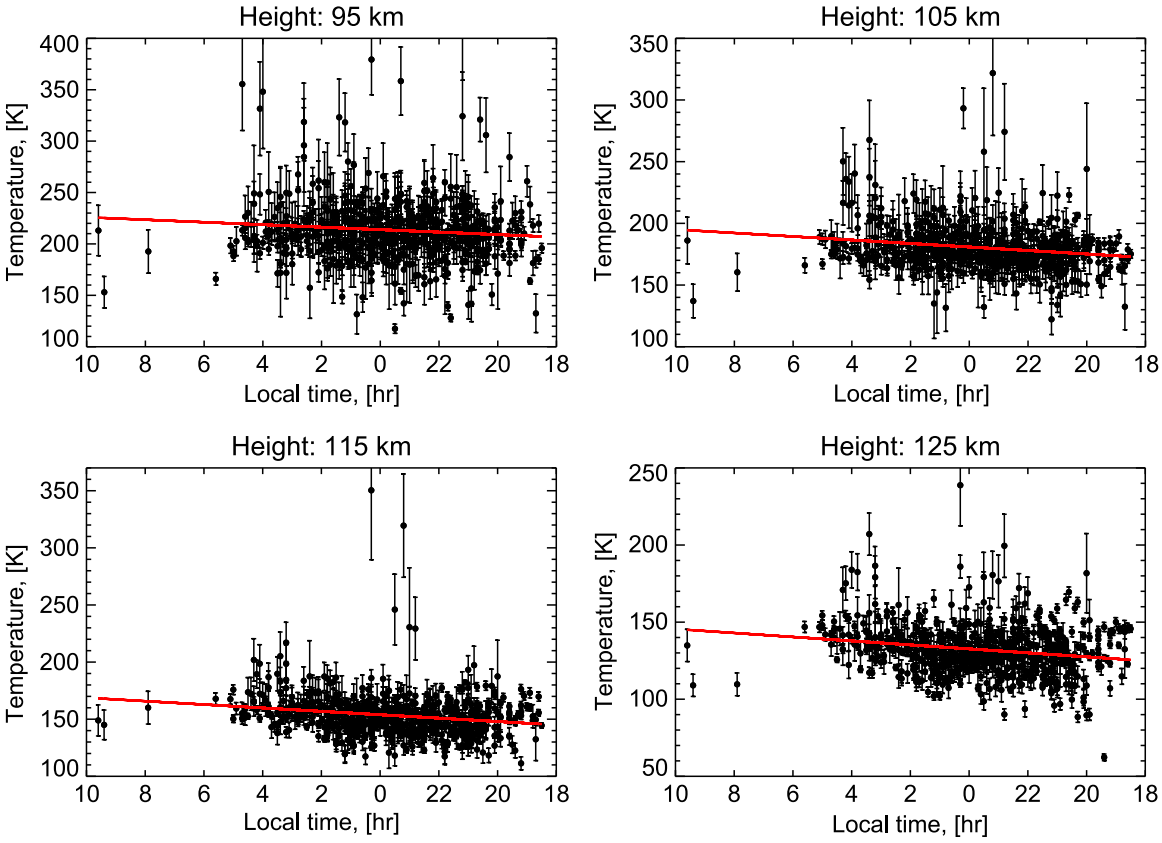

Fig. 7. Atmospheric temperature at constant altitudes as function of local time, together with the error values. Linear fitting curves are also shown (red lines). (For interpretation of the references to color in this figure caption, the reader is referred to the web version of this paper.)

it is taken from the Zasova model (Zasova et al., 2007, 2006) at altitudes of <100 km and from the VIRA model (Keating et al., 1985) for the altitude range 100–140 km.

As can be observed in Fig. 12, the homopause altitude derived by the SPICAV measurements varies between 119 and 138 km of altitude, exhibiting a high variability. The altitude shows a clear dependence on the local solar time with higher values on the morning side compared to the evening side. The dependence on the latitude is more difficult to analyze due to the scarcity of data at middle/high latitudes. Values of the homopause altitude are in good agreement with previous measurements (Mahieux et al., 2012; de Pater and Lissauer, 2001; von Zahn et al., 1980).

7. Comparison with literature

In order to study the latitudinal and local time behavior, and to exclude orbit-to-orbit variations, SPICAV temperature profiles have been grouped in latitudinal and local time bins and for each bin the mean vertical temperature profile and its standard deviation were computed. The list of the latitudinal and local time bins defined for this study is shown in Table 1. Latitudinal and local time groups were chosen in order to have at least five measurements in each bin. Average temperature profiles for different latitudinal and local time bins are displayed in Fig. 13.

At high latitudes (60–90°) temperature profiles do not show any clear dependence on local time, however this could be also explained by the limited number of local time bins (Fig. 13F). At midlatitudes (30–60°) for both hemispheres above ~ 110 km a decrease of temperatures with local time can be observed; below this altitude no clear trend can be seen (Fig. 13A and E). In the 10/30° and $-30/-10°$ latitudinal regions a stronger dependence on local time is observed (Fig. 13B and D). In the northern hemisphere, below ~ 125 km of height, the temperatures increase from 01:00 to 06:00 h. Above this altitude temperatures generally decrease with increasing local time. In the southern hemisphere temperatures exhibit a significantly larger variability compared to the northern hemisphere: temperatures increase of ~ 40 K from 18:00 to 05:00 h. In the equatorial region ($-10/10°$) SPICAV temperatures do not show any variation with local time between 90 and 120 km of altitude (Fig. 13C). However, above 120 km a decrease of temperature (≤ 10 K) with local time can be seen.

Whenever possible, SPICAV temperature profiles were compared to previous measurements, acquired both from spacecraft and ground-based observations. Here we present few examples of average temperature profiles for the latitudinal ranges 10/30°N and $-10/-30$°S (Figs. 14 and 15). A detailed description of SPICAV average temperature profiles for all latitude and local time bins is available as online Supplementary material.

For all latitudes and local times, SPICAV temperatures in the 90–100 km altitude region appear warmer (~ 30 K) compared to the Zasova model (Zasova et al., 2007, 2006).

In the 10/30° and $-30/-10°$ latitudinal regions a good agreement with the VIRA and VTS3 models is observed for both hemispheres above ~ 105 km; the discrepancy between the SPICAV temperatures and the two models increases with local time, especially on the morning side (Figs. 14 and 15). It should be noted that the VIRA model is obtained while averaging over all latitudes and nighttime 19:00–05:00 h local times while the VTS3 model is derived for midnight at the equator. This could explain some of the observed discrepancies. In addition, both the VIRA and VTS3 models below 140 km are dependent on theory and on extrapolation since data at these altitudes were sparse (Keating et al., 1985).

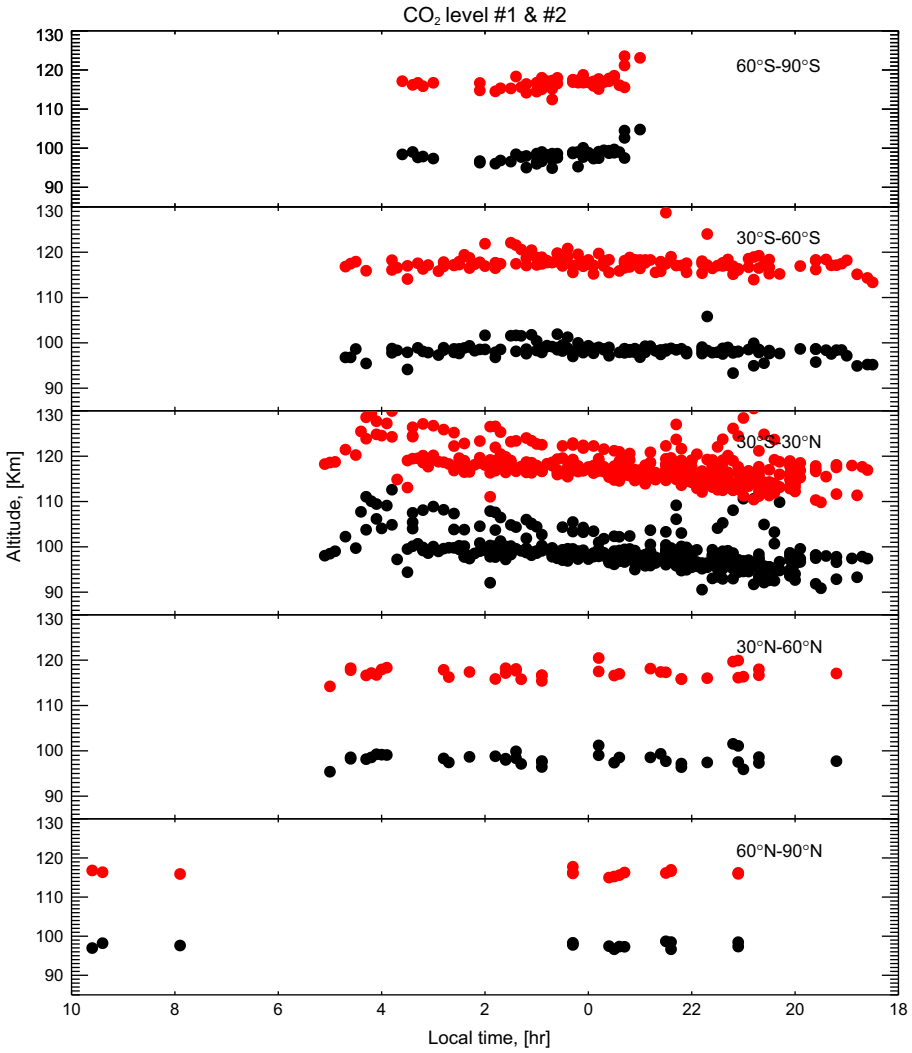

Fig. 8. Altitude of two CO_2 density levels as a function of the local solar time for different latitudinal bins. Black dots correspond to the CO_2 mass density level of 10^{-4} kg m^{-3}, while red dots correspond to a mass density of 10^{-6} kg m^{-3}. (For interpretation of the references to color in this figure caption, the reader is referred to the web version of this paper.)

Comparison with the SOIR/VEx temperature profiles is possible only close to the terminator (SZA=90°). In order to exclude orbit-to-orbit variability, SPICAV profiles are compared to SOIR mean temperature profiles from the VAST (Venus Atmosphere From SOIR Measurements at the Terminator) compilation (Mahieux et al., 2012, 2015). In the northern hemisphere SOIR temperature profiles exhibit a warm region in a slightly higher altitude region (100–110 km) compared to SPICAV temperatures. A good agreement is observed at 130 km in the local time range 18:00–20:00 h where both SPICAV and SOIR temperatures reach a minimum value of ~140 K (Fig. 14). On the morning side of the terminator SOIR temperature profile shows a cold layer, with temperature less than 120 ± 25 K, which is not reached by the SPICAV temperature (Fig. 14). A good agreement is observed between the SPICAV and SOIR measurements in the southern hemisphere on the evening side of the terminator (Fig. 15). The comparison with ground-based measurement (Clancy et al., 2012) is very good in both hemispheres for the local times 18:00–02:00 h; between 02:00 and 06:00 h SPICAV temperatures are warmer than the sub-mm profile by about 20–30 K on average. SPICAV mean temperature profiles are compared also with the OIR sounding measurements (Taylor et al., 1980) in the local time range 04:00–06:00 h on the northern hemisphere, and with the Pioneer Venus (PV) night probe (Seiff and Kirk, 1982) in the local time range 00:00–01:00 h on the southern hemisphere. SPICAV temperatures are warmer (~50 K) compared to the Pioneer Venus data. Comparison with temperature profiles acquired by the radio-occultation experiment VeRa/VEx is possible only in a small height range (90–95 km). At these altitudes, however, VeRa profiles are still strongly dependent on the upper boundary condition, which has to be implemented at an altitude of 100 km (Tellmann et al., 2009; Piccialli et al., 2012). Single VeRa profiles are used for the comparisons. Potential differences between SPICAV and VeRa might therefore be at least partially caused by day-to-day variations in the VeRa profiles.

8. Summary and conclusions

Observations acquired by the SPICAV-UV experiment in the stellar occultation mode were used to investigate the thermal structure of Venus upper atmosphere (90–140 km). In total, more than 587 vertical profiles of CO_2 local density and temperature were retrieved with a vertical resolution ranging from 500 m to ~7 km. They cover both the southern and the northern hemispheres on the nightside (6 pm–6 am local time). The main features observed in the temperature structure are (i) the warmer layer at 90–100 km altitude, (ii) the constant decrease of temperature with altitude reaching minimum values of ~100–130 K

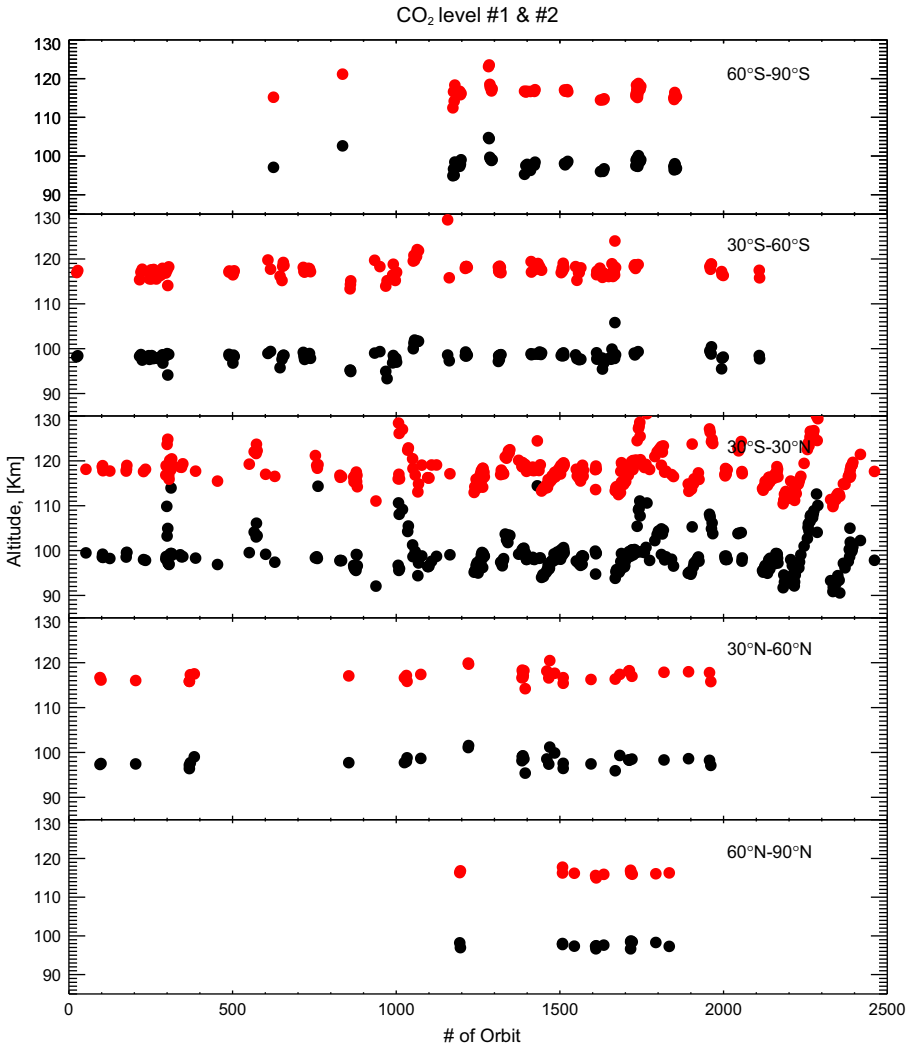

Fig. 9. Altitude of two CO_2 density levels as function of orbit number for different latitudinal bins. Black dots correspond to the CO_2 density level of 10^{-4} kg m^{-3}, while red dots correspond to a density of 10^{-6} kg m^{-3}. (For interpretation of the references to color in this figure caption, the reader is referred to the web version of this paper.)

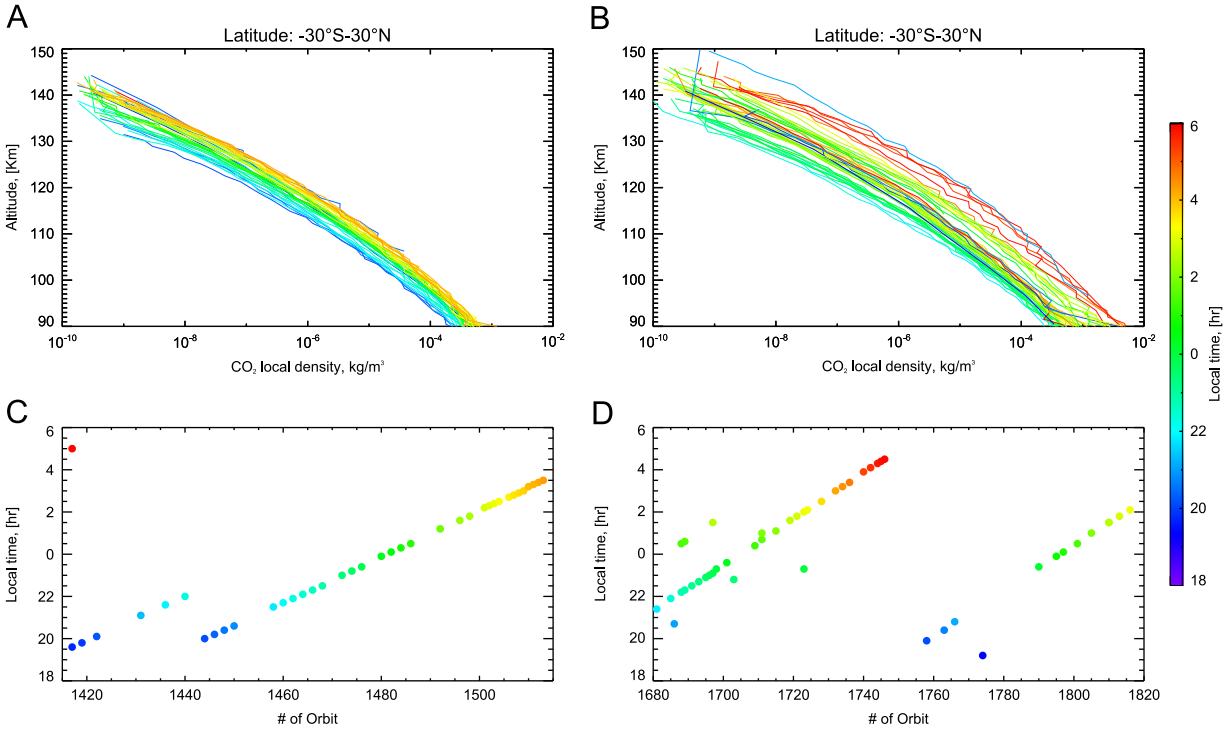

Fig. 10. The two panels at the top (A and B) show CO_2 density profiles. Bottom panels (C and D) give the local solar time and orbit number of the CO_2 density profiles presented respectively in figures A and B. The color code is the same in all panels, and it is the local solar time: evening measurements are bluish, while morning measurements are reddish. (For interpretation of the references to color in this figure caption, the reader is referred to the web version of this paper.)

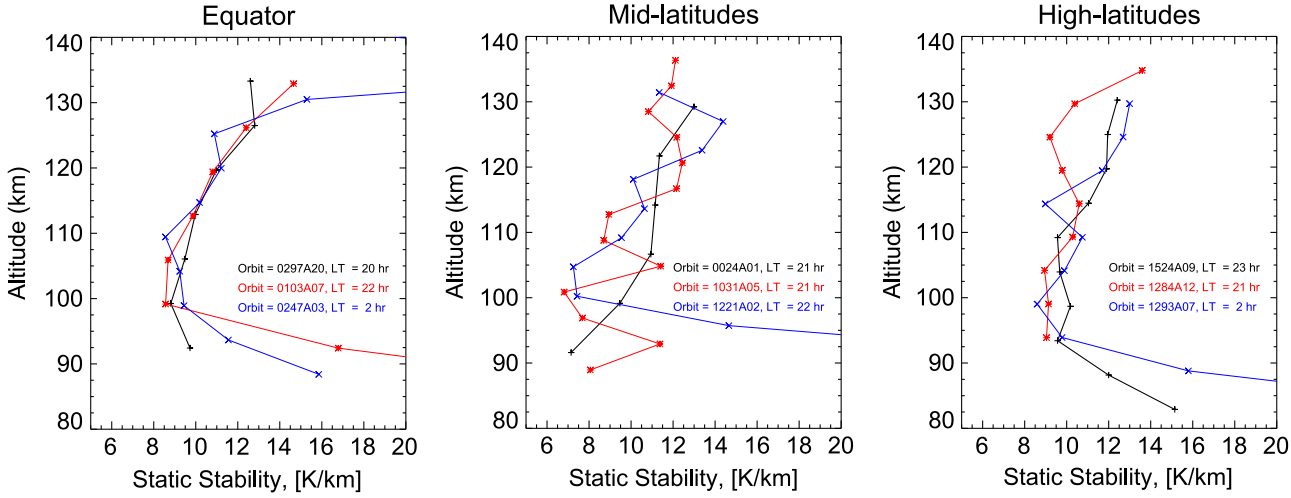

Fig. 11. Vertical profiles of static stability $dT/dz - \Gamma_d$, (K/km). Panels correspond respectively to (Left) equatorial latitudes; (middle) mid-latitudes; and (right) high latitudes.

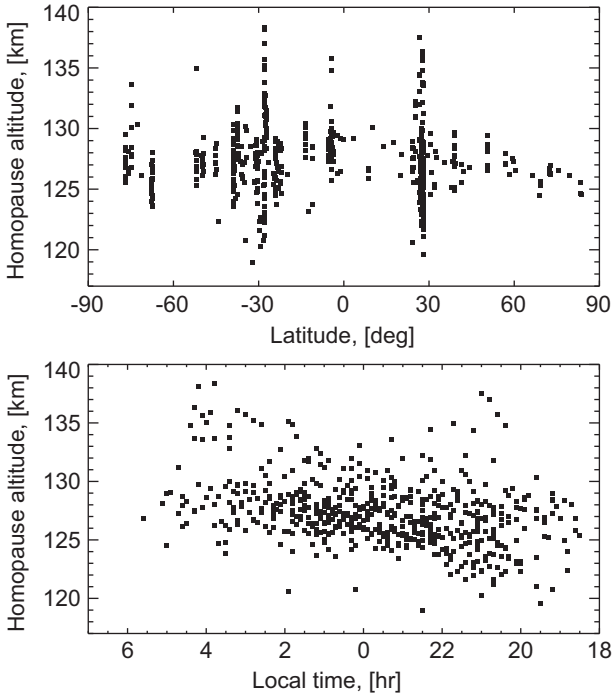

Fig. 12. Homopause altitudes derived from SPICAV data as a function of latitude (Top) and local solar time (Bottom).

above 120 km altitude. In good agreement with previous observations (Migliorini et al., 2012; Mahieux et al., 2012), SPICAV thermal structure exhibits a symmetry in terms of latitude between the two hemispheres. Local time variations dominate the thermal structure of Venus upper atmosphere in this altitude range: temperature is ~20 K warmer at dawn compared to dusk. VIRTIS as well as Venera 15 temperature retrievals present a similar trend: air temperature is colder during the evening than at morning above 10 mbar (~76 km) (Zasova et al., 2007; Grassi et al., 2010; Migliorini et al., 2012). Furthermore, a significant variability both on day-to-day and longer timescales affects the thermal structure of Venus upper mesosphere/lower thermosphere. Temperatures can display variations of ~10 K on timescales of 24 h up to ~50 K on timescales of few (Earth) months; previous observations also reported such strong variations (Roos-Serote et al., 1995; Rengel et al., 2008; Clancy et al., 2012; Mahieux et al., 2012, 2015; Sonnabend et al., 2012). The altitude region between 70 and 120 km acts as a transition zone in which the two major dynamic regimes are superimposed and it is characterized by strong turbulence. A general circulation model developed by Hoshino et al. (2012) suggests that Kelvin waves may propagate in the mesosphere up to 130 km and induce temporal variability into

Table 1
Summary of the latitude and local time groups defined for this study.

Latitude range (deg)	Local time range (h)	Number of orbits
60/90°	18:00–24:00	10
30/60°	19:00–22:00	8
	22:00–24:00	9
	00:00–02:00	10
	02:00–04:00	5
	04:00–06:00	7
10/30°	18:00–20:00	12
	20:00–21:00	19
	21:00–22:00	20
	22:00–23:00	29
	23:00–24:00	18
	00:00–01:00	24
	01:00–02:00	25
	02:00–03:00	16
	03:00–04:00	15
	04:00–06:00	10
−10/10°	19:00–21:00	17
	21:00–22:00	13
	22:00–24:00	6
	01:00–02:00	5
−30/−10°	18:00–20:00	7
	20:00–21:00	13
	21:00–22:00	17
	22:00–23:00	24
	23:00–24:00	17
	00:00–01:00	10
	01:00–02:00	11
	02:00–03:00	6
	03:00–05:00	6
−60/−30°	18:00–19:00	5
	19:00–20:00	8
	20:00–21:00	13
	21:00–22:00	16
	22:00–23:00	17
	23:00–24:00	18
	00:00–01:00	23
	01:00–02:00	12
	02:00–03:00	12
	03:00–05:00	12
−90/−60°	22:00–24:00	14
	00:00–02:00	26
	02:00–04:00	7

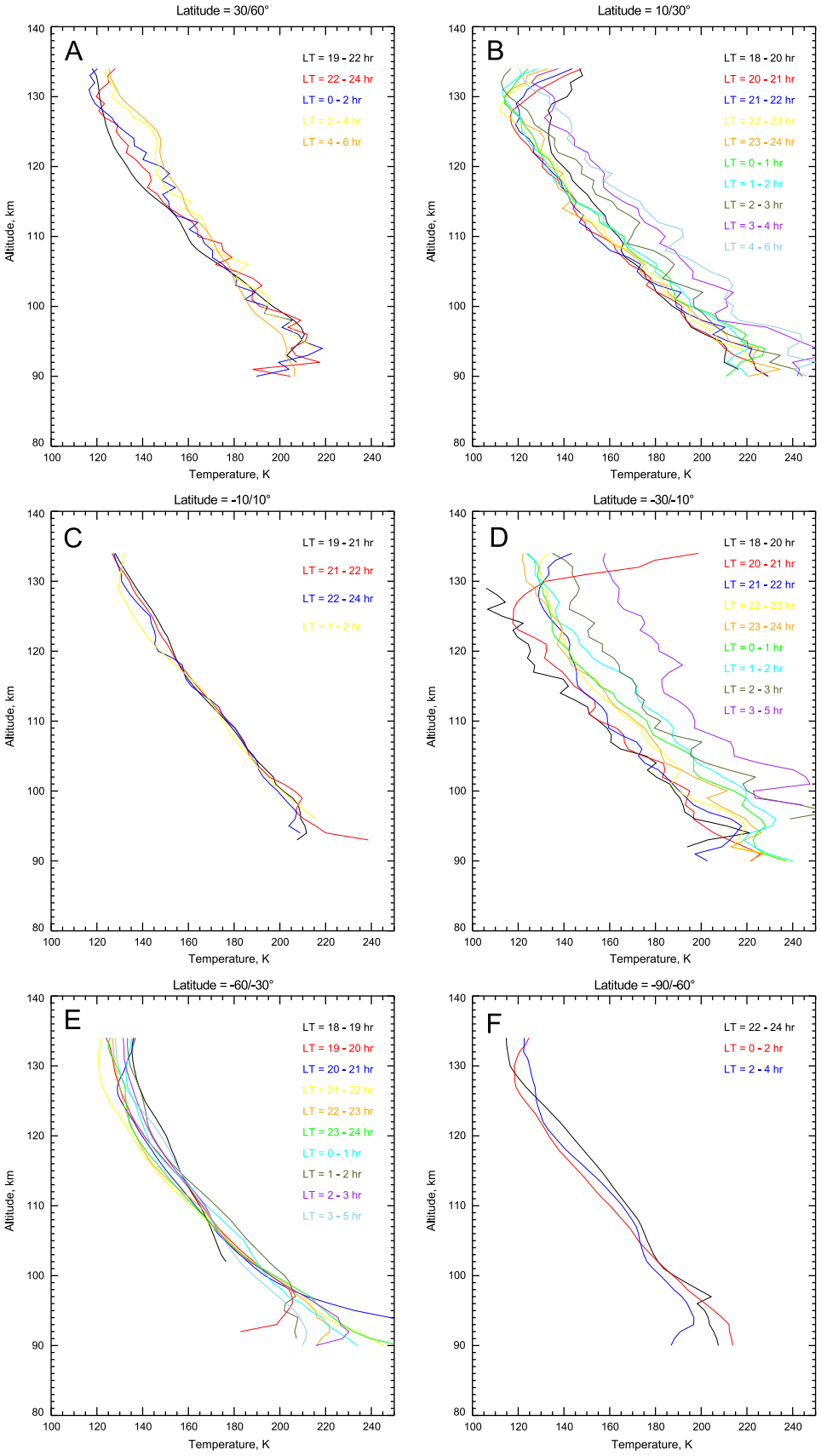

Fig. 13. SPICAV average temperature profiles for the different latitudinal bins: (A) 30/60°; (B) 10/30°; (C) −10/10°; (D) −30/−10°; (E) −60/−30°; (F) −90/−60°. Different colors correspond to different local times (LT). (For interpretation of the references to color in this figure caption, the reader is referred to the web version of this paper.)

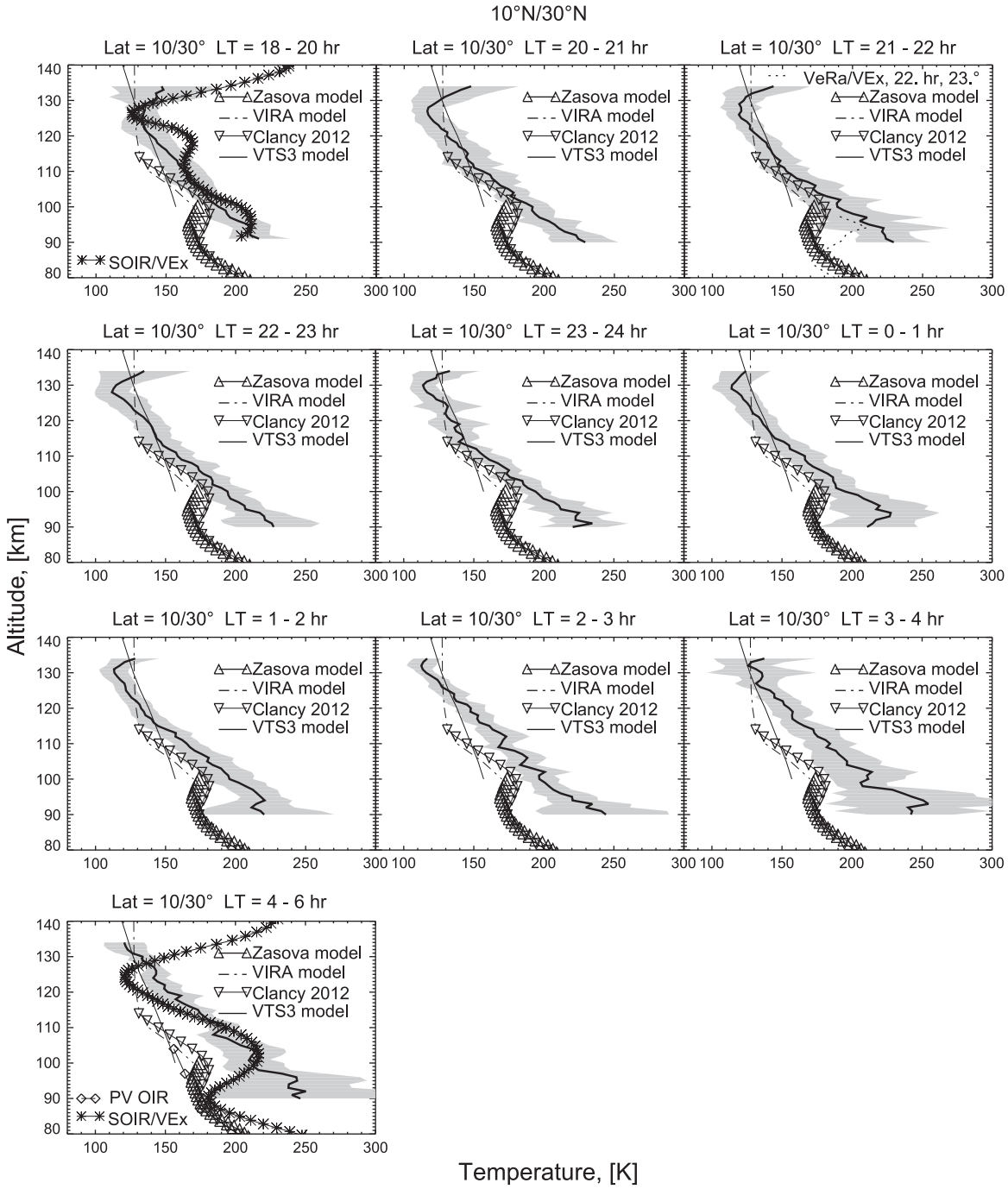

Fig. 14. SPICAV average vertical temperature profiles (thick black lines) in the 10–30°N latitude region for different local times (LT). The gray envelope is the standard deviation. The Zasova (Zasova et al., 2007, 2006), the VIRA (Keating et al., 1985) and the VTS3 (Hedin et al., 1983) models are indicated respectively by triangle symbols, the dash-dotted line, and the dashed line. Vertical temperature profiles acquired by the radio-occultation experiment VeRa/VEx (dot line), the OIR sounding measurements (diamond symbols), and the solar-occultation experiment SOIR/VEx (asterisk symbols) are also shown (Taylor et al., 1980; Tellmann et al., 2009; Mahieux et al., 2012). Sub-mm ground-based observations are also displayed (downward triangle symbols) (Clancy et al., 2012).

the nightglow and thermal structure of the lower thermosphere. In addition, Bougher et al. (2015) point out the importance of incorporating upward propagating thermal tides and planetary waves together with gravity wave breaking in their Venus Thermospheric General Circulation Model (VTGCM) in order to better address the variability observed in the upper atmosphere.

SPICAV temperature profiles were averaged over several latitudinal and local time bins in order to exclude the influence of orbit-to-orbit variations, and mean profiles were then compared to measurements obtained from ground-based observations (Rengel et al., 2008; Clancy et al., 2012), previous spacecraft missions (Seiff et al., 1980; Seiff and Kirk, 1982; Taylor et al., 1980; Zasova et al., 2007) and the Venus Express mission (Tellmann et al., 2009; Mahieux et al., 2012). Average temperature profiles are generally in agreement with the literature data above ~100 km altitude. Below this altitude, SPICAV thermal structure exhibits a warm layer with values reaching ~250 K at about 90 km which was interpreted as the result of adiabatic warming due to air subsidence on the nightside (Bertaux et al., 2007b). This observation is in agreement with VTGCM simulations that indicate that the nightside warm temperature bulge may be connected dynamically to dayside peak temperatures at $\sim 115 \pm 5$ km (Brecht et al., 2012). Brecht et al. (2012) suggest that the day-to-night

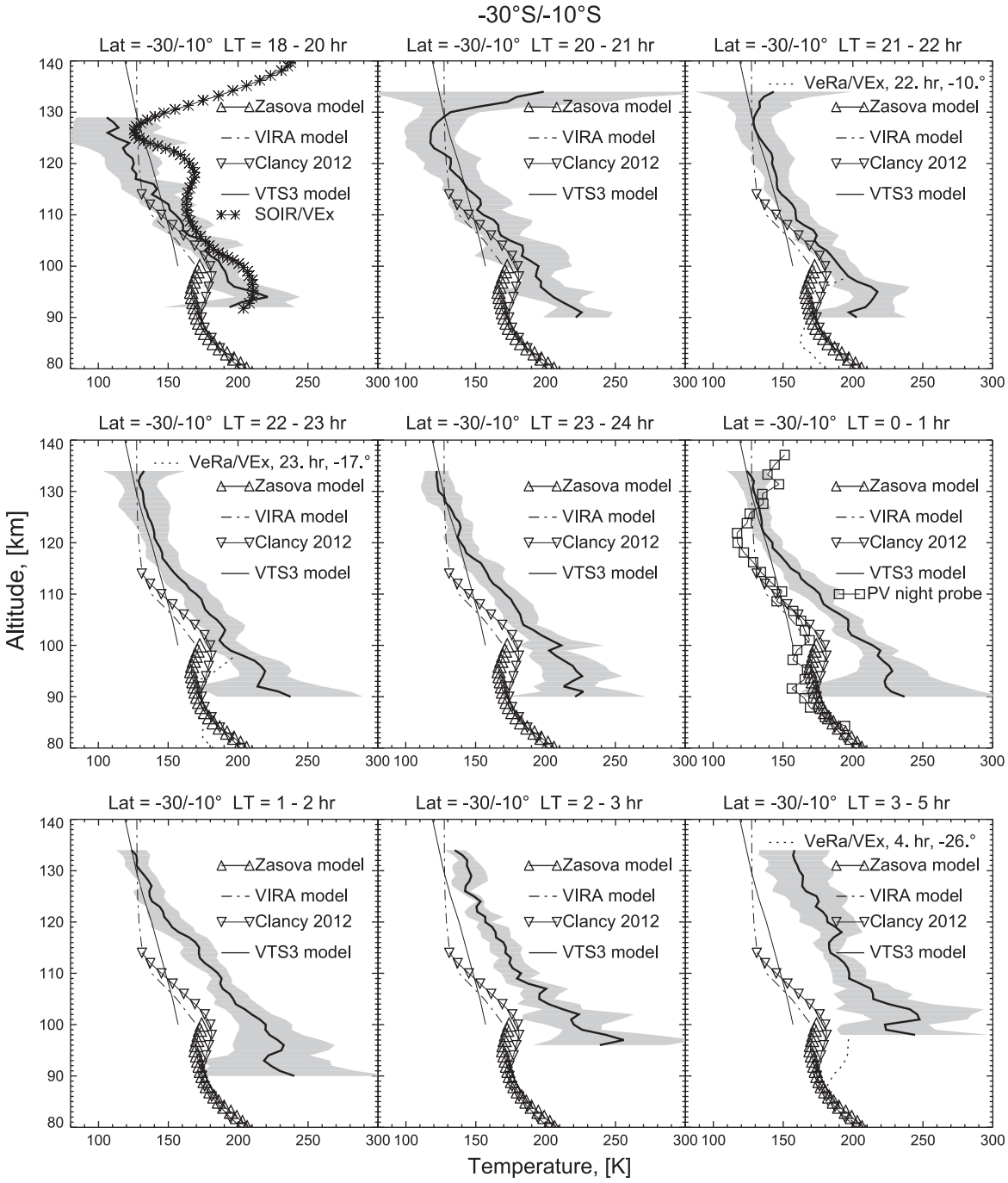

Fig. 15. SPICAV average vertical temperature profiles (thick black lines) in the −10 to −30°S latitude region for different local times (LT). The gray envelope is the standard deviation. The Zasova (Zasova et al., 2007, 2006), the VIRA (Keating et al., 1985) and the VTS3 (Hedin et al., 1983) models are indicated respectively by triangle symbols, the dash-dotted line, and the dashed line. Vertical temperature profiles acquired by the radio-occultation experiment VeRa/VEx (dot line), the Pioneer Venus descent night probe (square symbols), ground-based observation (downward triangle symbols), and the solar-occultation experiment SOIR/VEx (asterisk symbols) are also shown (Seiff and Kirk, 1982; Tellmann et al., 2009; Clancy et al., 2012; Mahieux et al., 2012).

circulation from the warm dayside region produces downwelling winds on the nightside resulting in adiabatic heating at about 90–100 km. The CO_2 homopause altitude was retrieved; it varies between 119 and 138 km of altitude in good agreement with previous observations (Mahieux et al., 2012; de Pater and Lissauer, 2001; von Zahn et al., 1980), and it exhibits a high variability. A strong dependence of the altitude on the local time is observed, with higher values at dawn compared to dusk.

This work is opened to further development. The increase of the SPICAV database and the comparison to new measurements acquired by the Venus Express instruments as well as ground-based observations are necessary to obtain a better understanding of the strong variability observed in Venus upper atmosphere. Moreover recently, several experiments on board Venus Express have reported detection of waves in the Venus atmosphere both as oscillations on the temperature field and as patterns on the cloud layer (Tellmann et al., 2012; Piccialli et al., 2014). SPICAV-UV, with a vertical resolution of 1–7 km, may offer the possibility to study wavelike variations on the vertical profiles of temperature and density.

Acknowledgments

We wish to thank the two anonymous reviewers for their careful reading of the manuscript and their suggestions for making this a stronger paper. A. Piccialli acknowledges funding from the European Union Seventh Framework Programme (FP7/2007-2013) under Grant agreement no. 246556.

A. Fedorova, O. Korablev and D. Belyaev acknowledge the Grant 11.G34.31.0074 from the Russian government and the program 22 from the RAS.

The research program was supported by the Belgian Federal Science Policy Office and the European Space Agency (ESA, PRODEX program, Contracts C 90268, 90113, and 17645). We acknowledge the support of the Interuniversity Attraction Poles program financed by the Belgian government (Planet TOPERS). A. Mahieux thanks the FNRS for the position of chargé de recherche.

The authors acknowledge the support provided by ISSI, through the organization of the International Team "Towards a self-consistent model of the thermal structure of the Venus atmosphere" (http://www.issibern.ch/teams/venusatmos/).

Appendix A. Supplementary data

Supplementary data associated with this paper can be found in the online version at http://dx.doi.org/10.1016/j.pss.2014.12.009.

References

Belyaev, D.A., Montmessin, F., Bertaux, J.L., Mahieux, A., Fedorova, A.A., Korablev, O.I., Marcq, E., Yung, Y.L., Zhang, X., 2012. Vertical profiling of SO_2 and SO above Venus' clouds by SPICAV/SOIR solar occultations. Icarus 217, 740–751.

Bertaux, J.L., Nevejans, D., Korablev, O., Villard, E., Quémerais, E., Neefs, E., Montmessin, F., Leblanc, F., Dubois, J.P., Dimarellis, E., Hauchecorne, A., Lefèvre, F., Rannou, P., Chaufray, J.Y., Cabane, M., Cernogora, G., Souchon, G., Semelin, F., Reberac, A., van Ransbeek, E., Berkenbosch, S., Clairquin, R., Muller, C., Forget, F., Hourdin, F., Talagrand, O., Rodin, A., Fedorova, A., Stepanov, A., Vinogradov, I., Kiselev, A., Kalinnikov, Y., Durry, G., Sandel, B., Stern, A., Gérard, J.C., 2007a. SPICAV on Venus express: three spectrometers to study the global structure and composition of the Venus atmosphere. Planet. Space Sci. 55, 1673–1700.

Bertaux, J.L., Vandaele, A.C., Korablev, O., Villard, E., Fedorova, A., Fussen, D., Quémerais, E., Belyaev, D., Mahieux, A., Montmessin, F., Muller, C., Neefs, E., Nevejans, D., Wilquet, V., Dubois, J.P., Hauchecorne, A., Stepanov, A., Vinogradov, I., Rodin, A., Bertaux, J.L., Nevejans, D., Korablev, O., Montmessin, F., Vandaele, A.C., Fedorova, A., Cabane, M., Chassefière, E., Chaufray, J.Y., Dimarellis, E., Dubois, J.P., Hauchecorne, A., Leblanc, F., Lefèvre, F., Rannou, P., Quémerais, E., Villard, E., Fussen, D., Muller, C., Neefs, E., van Ransbeeck, E., Wilquet, V., Rodin, A., Stepanov, A, Vinogradov, I., Zasova, L., Forget, F., Lebonnois, S., Titov, D., Rafkin, S., Durry, G., Gérard, J.C., Sandel, B., 2007b. A warm layer in Venus' cryosphere and high-altitude measurements of HF, HCl, H_2O and HDO. Nature 450, 646–649.

Bougher, S.W., Brecht, A.S., Schulte, R., Fischer, J.L., Parkinson, C.D., Mahieux, A., Wilquet, V., Vandaele, A.C., 2015. Upper atmosphere temperature structure at the Venusian terminators: a comparison of SOIR and VTGCM results. Submitted to Planetary and Space Science 113-114, 337–347.

Brecht, A.S., Bougher, S.W., Gérard, J.C., Soret, L., 2012. Atomic oxygen distributions in the Venus thermosphere: comparisons between Venus express observations and global model simulations. Icarus 217, 759–766.

Clancy, R.T., Muhleman, D.O., 1991. Long-term (1979–1990) changes in the thermal, dynamical, and compositional structure of the Venus mesosphere as inferred from microwave spectral line observations of C-12O, C-13O, and CO-18. Icarus 89, 129–146.

Clancy, R.T., Sandor, B.J., Moriarty-Schieven, G., 2012. Thermal structure and CO distribution for the Venus mesosphere/lower thermosphere: 2001–2009 inferior conjunction sub-millimeter CO absorption line observations. Icarus 217, 779–793.

Clancy, R.T., Sandor, B.J., Moriarty-Schieven, G.H., 2003. Observational definition of the Venus mesopause: vertical structure, diurnal variation, and temporal instability. Icarus 161, 1–16.

Clancy, R.T., Sandor, B.J., Moriarty-Schieven, G.H., 2008. Venus upper atmospheric CO, temperature, and winds across the afternoon/evening terminator from June 2007 JCMT sub-millimeter line observations. Planet. Space Sci. 56, 1344–1354.

de Pater, I., Lissauer, J.J., 2001. Planetary Sciences, 2nd ed. Cambridge University Press, Cambridge.

Esposito, L.W., Bertaux, J., Krasnopolsky, V., Moroz, V.I., Zasova, L.V., 1997. Chemistry of lower atmosphere and clouds. In: Bougher, S.W., Hunten, D.M., Philips, R.J. (Eds.), Venus II: Geology, Geophysics, Atmosphere, and Solar Wind Environment, p. 415.

Forget, F., Montmessin, F., Bertaux, J.L., González-Galindo, F., Lebonnois, S., Quémerais, E., Reberac, A., Dimarellis, E., López-Valverde, M.A., 2009. Density and temperatures of the upper Martian atmosphere measured by stellar occultations with Mars Express SPICAM. J. Geophys. Res. (Planets) 114, 1004.

Grassi, D., Migliorini, A., Montabone, L., Lebonnois, S., Cardesìn-Moinelo, A., Piccioni, G., Drossart, P., Zasova, L.V., 2010. Thermal structure of Venusian nighttime mesosphere as observed by VIRTIS-Venus Express. J. Geophys. Res. (Planets) 115, 9007.

Hedin, A.E., Niemann, H.B., Kasprzak, W.T., Seiff, A., 1983. Global empirical model of the Venus thermosphere. J. Geophys. Res. 88, 73–83.

Holton, J.R., 2004. An Introduction to Dynamic Meteorology. International Geophysics Series, 4th ed. Academic Press, San Diego, New York.

Hoshino, N., Fujiwara, H., Takagi, M., Takahashi, Y., Kasaba, Y., 2012. Characteristics of planetary-scale waves simulated by a new venusian mesosphere and thermosphere general circulation model. Icarus 217, 818–830.

Howell, S.B., 2006. Handbook of CCD Astronomy.

Keating, G.M., Bertaux, J.L., Bougher, S.W., Dickinson, R.E., Cravens, T.E., Hedin, A.E., 1985. Models of Venus neutral upper atmosphere—structure and composition. Adv. Space Res. 5, 117–171.

Kliore, A.J., Moroz, V.I., Keating, G.M., 1985. The Venus international reference atmosphere. Adv. Space Res. 5.

Lebonnois, S., Hourdin, F., Eymet, V., Crespin, A., Fournier, R., Forget, F., 2010. Superrotation of Venus' atmosphere analyzed with a full general circulation model. J. Geophys. Res. (Planets) 115, 6006.

Lee, Y.J., Titov, D.V., Tellmann, S., Piccialli, A., Ignatiev, N., Pätzold, M., Häusler, B., Piccioni, G., Drossart, P., 2012. Vertical structure of the Venus cloud top from the VeRa and VIRTIS observations onboard Venus Express. Icarus 217, 599–609.

Lellouch, E., Goldstein, J.J., Rosenqvist, J., Bougher, S.W., Paubert, G., 1994. Global circulation, thermal structure, and carbon monoxide distribution in Venus' mesosphere in 1991. Icarus 110, 315–339.

Mahieux, A., Vandaele, A.C., Bougher, S.W., Yelle, R.V., Drummond, R., Robert, S., Wilquet, V., Piccialli, A., Montmessin, F., Tellmann, S., Pätzold, M., Häusler, B., Bertaux, J.L., 2015. Update of the Venus density and temperature profiles at high altitude measured by SOIR on board Venus Express. Planet. Space Sci. 113-114, 310–321. http://dx.doi.org/10.1016/j.pss.2014.12.020.

Mahieux, A., Vandaele, A.C., Robert, S., Wilquet, V., Drummond, R., Montmessin, F., Bertaux, J.L., 2012. Densities and temperatures in the Venus mesosphere and lower thermosphere retrieved from SOIR on board venus express: carbon dioxide measurements at the Venus terminator. J. Geophys. Res. (Planets) 117, 7001.

Migliorini, A., Grassi, D., Montabone, L., Lebonnois, S., Drossart, P., Piccioni, G., 2012. Investigation of air temperature on the nightside of Venus derived from VIRTIS-H on board Venus-Express. Icarus 217, 640–647.

Montmessin, F., Bertaux, J.L., Lefèvre, F., Marcq, E., Belyaev, D., Gérard, J.C., Korablev, O., Fedorova, A., Sarago, V., Vandaele, A.C., 2011. A layer of ozone detected in the nightside upper atmosphere of Venus. Icarus 216, 82–85.

Montmessin, F., Quémerais, E., Bertaux, J.L., Korablev, O., Rannou, P., Lebonnois, S., 2006. Stellar occultations at UV wavelengths by the SPICAM instrument: retrieval and analysis of Martian haze profiles. J. Geophys. Res. (Planets) 111, 9.

Nagy, A.F., Balogh, A., Cravens, T.E., Mendillo, M., Mueller-Wodarg, I., 2009. Comparative aeronomy. In: Space Sciences Series of ISSI, vol. 29. Springer, New York.

Piccialli, A., Tellmann, S., Titov, D.V., Limaye, S.S., Khatuntsev, I.V., Pätzold, M., Häusler, B., 2012. Dynamical properties of the Venus mesosphere from the radio-occultation experiment VeRa onboard Venus Express. Icarus 217, 669–681.

Piccialli, A., Titov, D.V., Sanchez-Lavega, A., Peralta, J., Shalygina, O., Markiewicz, W.J., Svedhem, H., 2014. High latitude gravity waves at the Venus cloud tops as observed by the Venus Monitoring Camera on board Venus Express. Icarus 227, 94–111.

Quémerais, E., Bertaux, J.L., Korablev, O., Dimarellis, E., Cot, C., Sandel, B.R., Fussen, D., 2006. Stellar occultations observed by SPICAM on Mars Express. J. Geophys. Res. (Planets) 111, 9.

Rengel, M., Hartogh, P., Jarchow, C., 2008. HHSMT observations of the Venusian mesospheric temperature, winds, and CO abundance around the MESSENGER flyby. Planet. Space Sci. 56, 1688–1695 0810.2899.

Roos-Serote, M., Drossart, P., Encrenaz, T., Lellouch, E., Carlson, R.W., Baines, K.H., Taylor, F.W., Calcutt, S.B., 1995. The thermal structure and dynamics of the atmosphere of Venus between 70 and 90 km from the Galileo-NIMS spectra. Icarus 114, 300–309.

Royer, E., Montmessin, F., Bertaux, J.L., 2010. NO emissions as observed by SPICAV during stellar occultations. Planss 58, 1314–1326.

Sanchez-Lavega, A., 2011. An Introduction to Planetary Atmospheres. CRC Press, Taylor and Francis, Boca Raton.

Sánchez-Lavega, A., Hueso, R., Piccioni, G., Drossart, P., Peralta, J., Pérez-Hoyos, S., Wilson, C.F., Taylor, F.W., Baines, K.H., Luz, D., Erard, S., Lebonnois, S., 2008. Variable winds on Venus mapped in three dimensions. Geophys. Res. Lett. 35, 13204.

Schubert, G., Bougher, S.W., Covey, C.C., Del Genio, A.D., Grossman, A.S., Hollingsworth, J.L., Limaye, S.S., Young, R.E., 2007. Venus atmosphere dynamics: a continuing enigma. In: Esposito, L.W., Stofan, E.R., Cravens, Th.E. (Eds.), Exploring Venus as Terrestrial Planet, Geophysical Monograph Series, pp. 121–138.

Seiff, A., Kirk, D.B., 1982. Structure of the Venus mesosphere and lower thermosphere from measurements during entry of the Pioneer Venus probes. Icarus 49, 49–70.

Seiff, A., Kirk, D.B., Young, R.E., Blanchard, R.C., Findlay, J.T., Kelly, G.M., Sommer, S.C., 1980. Measurements of thermal structure and thermal contrasts in the atmosphere of Venus and related dynamical observations—results from the four Pioneer Venus probes. J. Geophys. Res. 85, 7903–7933.

Seiff, A., Schofield, J.T., Kliore, A.J., Taylor, F.W., Limaye, S.S., 1985. Models of the structure of the atmosphere of Venus from the surface to 100 kilometers altitude. Adv. Space Res. 5, 3–58.

Sonnabend, G., Krötz, P., Schmülling, F., Kostiuk, T., Goldstein, J., Sornig, M., Stupar, D., Livengood, T., Hewagama, T., Fast, K., Mahieux, A., 2012. Thermospheric/mesospheric temperatures on Venus: results from ground-based high-resolution spectroscopy of CO_2 in 1990/1991 and comparison to results from 2009 and between other techniques. Icarus 217, 856–862.

Svedhem, H., Titov, D., Taylor, F., Witasse, O., 2009. Venus express mission. J. Geophys. Res. Planets 114, 3–21.

Svedhem, H., Titov, D.V., McCoy, D., Lebreton, J.P., Barabash, S., Bertaux, J.L., Drossart, P., Formisano, V., Häusler, B., Korablev, O., Markiewicz, W.J., Nevejans, D., Pätzold, M., Piccioni, G., Zhang, T.L., Taylor, F.W., Lellouch, E., Koschny, D., Witasse, O., Eggel, H., Warhaut, M., Accomazzo, A., Rodriguez-Canabal, J., Fabrega, J., Schirmann, T., Clochet, A., Coradini, M., 2007. Venus express—the first European mission to venus. Planet. Space Sci. 55, 1636–1652.

Taylor, F.W., Beer, R., Chahine, M.T., Diner, D.J., Elson, L.S., Haskins, R.D., McCleese, D.J., Martonchik, J.V., Reichley, P.E., Bradley, S.P., Delderfield, J., Schofield, J.T., Farmer, C.B., Froidevaux, L., Leung, J., Coffey, M.T., Gille, J.C., 1980. Structure and meteorology of the middle atmosphere of Venus Infrared remote sensing from the Pioneer orbiter. J. Geophys. Res. 85, 7963–8006.

Tellmann, S., Häusler, B., Hinson, D.P., Tyler, G.L., Andert, T.P., Bird, M.K., Imamura, T., Pätzold, M., Remus, S., 2012. Small-scale temperature fluctuations seen by the VeRa radio science experiment on venus express. Icarus 221, 471–480.

Tellmann, S., Pätzold, M., Häusler, B., Bird, M.K., Tyler, G.L., 2009. Structure of the Venus neutral atmosphere as observed by the radio science experiment VeRa on venus express. J. Geophys. Res. (Planets) 114.

Titov, D.V., Svedhem, H., Taylor, F.W., Barabash, S., Bertaux, J.L., Drossart, P., Formisano, V., Häusler, B., Korablev, O., Markiewicz, W.J., Nevejans, D., Pätzold, M., Piccioni, G., Sauvaud, J.A., Zhang, T.L., Witasse, O., Gerard, J.C., Fedorov, A., Sanchez-Lavega, A., Helbert, J., Hoofs, R., 2009. Venus express: highlights of the nominal mission. Solar Syst. Res. 43, 185–209.

von Zahn, U., Fricke, K.H., Hunten, D.M., Krankowsky, D., Mauersberger, K., Nier, O.A., 1980. The upper atmosphere of Venus during morning conditions. J. Geophys. Res. 85, 7829–7840.

Wilquet, V., Fedorova, A., Montmessin, F., Drummond, R., Mahieux, A., Vandaele, A.C., Villard, E., Korablev, O., Bertaux, J.L., 2009. Preliminary characterization of the upper haze by SPICAV/SOIR solar occultation in UV to mid-IR onboard Venus Express. J. Geophys. Res. (Planets) 114, 0.

Zasova, L.V., Ignatiev, N., Khatuntsev, I., Linkin, V., 2007. Structure of the Venus atmosphere. Planet. Space Sci. 55, 1712–1728.

Zasova, L.V., Moroz, V.I., Linkin, V.M., Khatuntsev, I.V., Maiorov, B.S., 2006. Structure of the Venusian atmosphere from surface up to 100 km. Cosmic Res. 44, 364–383.